International Journal of Computer Assisted Radiology and Surgery
https://doi.org/10.1007/s11548-017-1699-x

ORIGINAL ARTICLE

# Nonlinear deformation of tractography in ultrasound-guided low-grade gliomas resection

Yiming Xiao[1,2] · Live Eikenes[3] · Ingerid Reinertsen[4,5] · Hassan Rivaz[1,2]

Received: 29 September 2017 / Accepted: 21 December 2017


## Abstract

**Purpose** In brain tumor surgeries, maximum removal of cancerous tissue without compromising normal brain functions can improve the patient's survival rate and therapeutic benefits. To achieve this, diffusion MRI and intra-operative ultrasound (iUS) can be highly instrumental. While diffusion MRI allows the visualization of white matter tracts and helps define the resection plan to best preserve the eloquent areas, iUS can effectively track the brain shift after craniotomy that often renders the pre-surgical plan invalid, ensuring the accuracy and safety of the intervention. Unfortunately, brain shift correction using iUS and automatic registration has never been shown for brain tractography so far despite its rising significance in brain tumor resection.

**Methods** We employed a correlation-ratio-based nonlinear registration algorithm to account for brain shift through MRI–iUS registration and used the recovered deformations to warp both the brain anatomy and tractography seen in pre-surgical plans. The overall technique was demonstrated retrospectively on four patients who underwent iUS-guided low-grade brain gliomas resection.

**Results** Through qualitative and quantitative evaluations, the preoperative MRI and iUS scans were well realigned after nonlinear registration, and the deformed brain tumor volumes and white matter tracts showed large displacements away from the pre-surgical plans.

**Conclusions** We are the first to demonstrate the technique to track nonlinear deformation of brain tractography using real clinical MRI and iUS data, and the results confirm the need for updating white matter tracts due to tissue shift during surgery.

**Keywords** Intra-operative ultrasound · MRI · Brain tumor · Registration · Tractography · Neurosurgery · Brain shift

## Introduction

Gliomas are the most common central nervous system (CNS) tumors in adults [1], accounting for 80% of primary malignant brain tumors [2]. The World Health Organization (WHO) [3] divides gliomas into four grades based on their histological characters. High-grade gliomas are composed of various rapidly growing glial tumors of grade III and IV pathologies, with glioblastoma multiforme (grade IV) being the most malignant. Low-grade gliomas (grades I and II) are less aggressive, but without proper management, they will progress to high-grade tumors and eventually lead to death. Currently, surgery is the most common initial treatment choice for brain tumors, and resection at early stages has shown positive influence on the patients' survival rate [4–6].

Modern brain tumor resections aim to remove the maximum amount of cancerous tissue while keeping the brain functions intact. Nevertheless, to achieve this, two main challenges remain. First, many tumors contain or are right adjacent to eloquent areas that are closely associated with the patient's normal functions [7,8]. Ideal surgical plans should

✉ Yiming Xiao
yiming.xiao@concordia.ca

1 PERFORM Centre, Concordia University, Rm 2.211, 7200 Sherbrooke St. W., Montreal, QC H4B 1R6, Canada

2 Department of Electrical and Computer Engineering, Concordia University, Montreal, Canada

3 Department of Circulation and Medical Imaging, Norwegian University of Science and Technology, Trondheim, Norway

4 Department of Medical Technology, SINTEF, Trondheim, Norway

5 Norwegian National Advisory Unit for Ultrasound and Image-Guided Therapy, St. Olavs University Hospital, Trondheim, Norway

Published online: 03 January 2018

carefully balance the extent of tumor removal and the risk of damaging surrounding functional regions. Second, after craniotomy, brain tissue deformation (called brain shift) [9–11] can often move the anatomy of the tumor and other vital structures, such as blood vessels, due to intracranial pressure change, drug administration, tissue removal, and so on. Unfortunately, this displacement is usually not directly visible to the surgeons and can render the pre-surgical plan invalid, potentially compromising the safety and quality of the procedure.

Routine structural MR images (i.e., T1w or T2w FLAIR images) can depict the extents of brain tumors and their spatial relationship to other crucial structures (e.g., blood vessels). However, they fail to provide the functional relationship between the neoplastic mass and the normal brain structures to help achieve a maximal tumor resection without causing neurological deterioration. Functional MRI (fMRI) [12–14] allows the identification of important functional regions that may be invaded by the tumor. Unfortunately, it primarily focuses on the cortical structures, instead of the white matter, where gliomas often grow diffusely. Diffusion imaging can provide the information on the involvement and integrity of the white matter tracts within or surrounding the tumors, often in the form of tractography in surgical planning. Nowadays, the technique has been increasingly employed to investigate pathological changes of the brain tumors [8,15–17] and to help determine tumor grades and the extent of resection [7,18,19].

To monitor tissue shift and resection progression, intra-operative imaging methods, such as intra-operative magnetic resonance images (MRI) [11,20,21] and ultrasound (US) [10,13], are highly instrumental. Although intra-operative MRI can provide easier-to-comprehend image contrasts and the possibility of various MRI sequences to capture the dynamic structural, physiological, and functional changes during surgeries [20,21], it has a prohibitively high cost and requires MRI-compatible operating room and tools. In contrast, intra-operative ultrasound is portable, convenient, and real time. In addition, tumors can often be delineated in US even when they are not distinguishable from normal tissues under the microscope [22,23]. This can facilitate accurate resection, resulting in better surgical outcomes. In the presence of brain shift, by aligning the preoperative MRI with intra-operative ultrasound scans through automatic image registration algorithms [24–38], the deformation can be recovered to update the surgical plan, thus ensuring the quality of resection. Furthermore, as the surgeon's experience with intra-operative ultrasound varies and the ultrasound images often have limited field of view, it is difficult to interpret the information in intra-operative ultrasound. Correct MRI–US alignment can provide the surgeons the necessary overview of the surgical field and help them better interpret the ultrasound images.

Previously, there have been a number of direct and indirect techniques to tackle MRI–US registration in neurosurgery. For the indirect methods [24–33] images of different modalities are transformed into the same or similar feature space for registration. Roche et al. [24] performed a parametric polynomial fit of US intensity as a function of MR and its gradient to construct the functional correlation ratio (CR) similarity metric. Mercier et al. [25] and Arbel et al. [26] generated pseudo-US images by assigning corresponding image intensities seen in US scans to segmented MR images and then used the ANIMAL registration method [27] to align the resulting pseudo-US to real US scans. Similarly, Kuklisova-Murgasova et al. [28] proposed to employ an atlas to perform MRI segmentation for generating US-like images and then perform the registration with a uni-modal block-matching technique. Mellor and Brady [29] used mutual information (MI) of local phase information for MRI–US registration. De Nigris et al. [30] achieved the inter-modality registration through the alignment of the orientations of image gradients. Instead of employing the full images, potent anatomical features can be extracted as surrogates to register the entire images. Reinertsen et al. [31,32] used blood vessel features to register US and MR, while Coupé et al. [33] used the hyper-echogenic cerebral falx and the sulci structures in the brain US and MR images. More conveniently, direct approaches [34–38] optimize various metrics to directly align inter-modality images. Ji et al. [34] used normalized mutual information with selected US pixels for MRI–US registration. Wein et al. [35] and Fuerst et al. [36] used a Linear Correlation of Linear Combination ($LC^2$)-based similarity metric. Ferrante and Paragios [37] registered 2D US images to 3D MR volume using discrete optimization within a Markov random field framework. More recently, Rivaz et al. [38] proposed the Robust PaTch-based cOrrelation Ratio (RaPTOR) based on local correlation ratio [39] to perform direct nonlinear MRI–US registration. It has shown fast and robust performance in tracking tissue shift in brain tumor resection [38].

To date, inter-modal registration techniques [24–38] were employed only to update the structural images (e.g., aligning US to MRI) intra-operatively. Despite the rising new surgical paradigm to include functional data, there have been no reports on tissue shift correction for brain tractography in ultrasound-guided brain tumor resection. In this article, we employed surgical images from four patients who received low-grade brain gliomas resection to retrospectively demonstrate the application of intra-operative ultrasound to nonlinearly deform the tractography in the presence of brain shift. We employed RaPTOR [38] to recover the deformation through MRI–US registration and used the result to deform individuals' tractography. Our results showcased the feasibility and the necessity of intra-operatively updating brain tractography in tumor resection.

## Materials and methods

### Patients and MR imaging protocols

As a proof of concept, we selected four patients who received low-grade gliomas resection at St. Olavs University Hospital (Trondheim, Norway) to demonstrate our technique. The study was approved by the Regional Committee for Medical and Health Research Ethics in Central Norway, and all patients provided written informed consent prior to inclusion.

Preoperative MR images for all patients were acquired the day before surgery. All anatomical MRIs were acquired on a 3T Magnetom Skyra (Siemens, Erlangen, Germany) with a 20-channel head coil. The MRI protocol included a sagittal T1w Gd-enhanced sequence (TE = 2.96 ms, TR = 2000 ms, flip angle = 8°, 192 sagittal slices, acquisition matrix = 256 × 256, voxel size = 1.0 × 1.0 × 1.0 $mm^3$) and a sagittal T2w fluid-attenuated inversion recovery, or FLAIR (TE = 388 ms, TR = 5000 ms, flip angle = 120°, 192 sagittal slices, acquisition matrix = 256 × 256, voxel size = 1.0 × 1.0 × 1.0 $mm^3$) sequence.

For Patients 1, 2, and 3, the diffusion-weighted imaging (DWI) data were also obtained on the Skyra scanner with a 20-channel head coil, using a spin-echo echo-planar imaging (EPI) sequence (TE = 84 ms, TR = 6100 ms, matrix size = 96 × 96, voxel size = 2.5 × 2.5 × 2.5 $mm^3$ with 64 axial slices) with a gradient set containing 30 non-colinear directions of $b$ value = 1000 s/$mm^2$ and an image with $b$ value = 0 s/$mm^2$. For Patient 4, the DWI data were acquired on a Siemens Biograph mMR 3T PET/MRI scanner (Siemens Healthcare, Erlangen, Germany) with a 12-channel head/neck coil. The sequence (TR = 6700 ms, TE = 84 ms, acquisition matrix = 96 × 96 and image resolution = 3 × 3 × 3 $mm^3$ with 42 axial slices) was acquired in 30 encoding directions with $b$ = 1000 s/$mm^2$ and one image with $b$ value = 0 s/$mm^2$. For the DWI sequences on both scanners, the acquisitions were repeated twice for improving signal-to-noise ratio.

For surgical planning, the T1w and T2 FLAIR images were first co-registered and then rigidly registered to the DWI data. Prior to scanning, five fiducial markers were glued to the patient's head and were used for patient-to-image registration after head immobilization on the operating table. The brain tumors were manually segmented from the T2 FLAIR MRIs using ITK-SNAP (www.itksnap.org).

### Intra-operative ultrasound acquisition

Intra-operative ultrasound is routinely used for tumor resection at St. Olavs University Hospital. The setup for US acquisition in the operating room is shown in Fig. 1, where the ultrasound probe was covered with sterile probe drapes prior to image acquisition. The ultrasound images were acquired by the same surgeon using the Sonowand Invite neuronavigation system (Sonowand AS, Trondheim, Norway), which also contains a built-in Polaris camera (NDI, Waterloo, Canada) to capture the position and pose of the ultrasound probe via the optical trackers attached. The most commonly used probe was the 12FLA-L linear probe with a frequency range of 6–12 MHz and a footprint of 48 × 13 $mm^2$. For smaller superficial tumors, we used the 12FLA flat linear-array probe with a frequency range of 6–12 MHz and a footprint of 32 × 11 $mm^2$. The ultrasound probes were all factory-calibrated and equipped with removable sterilizable reference frames for optical tracking. The tracked 2D ultrasound data were reconstructed to 3D volumes using the built-in proprietary reconstruction method in the Sonowand Invite system, with a resolution between 0.14 × 0.14 × 0.14 $mm^3$ and 0.24 × 0.24 × 0.24 $mm^3$ depending on the probe types and imaging depth. All US volumes were inspected to have full tumor coverage and good image quality before saving in the navigation system, thus ensuring the consistency and quality of image acquisition across subjects. Although US images were obtained at different surgical stages, for this study, we only used the ultrasound volume acquired on the dura or the cortical surface right before resection started.

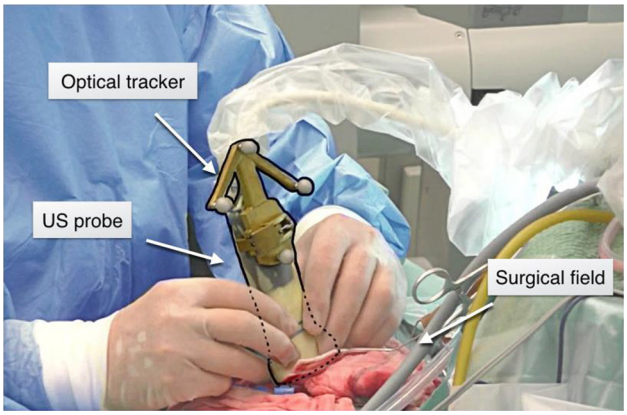


**Fig. 1** Intra-operative ultrasound image acquisitions during surgery. Ultrasound images were obtained using an optically tracked ultrasound transducer

## RaPTOR

We used RaPTOR [38], a technique based on correlation ratio [39] to recover brain shift. The correlation ratio (CR) for two images $X$ and $Y$, $\eta(Y|X)$, has a value in [0, 1], and is an asymmetric metric, i.e., $\eta(Y|X) \neq \eta(X|Y)$. Unlike the previous methods [24,39], RaPTOR estimates CR, $\eta(Y|X)$, through binning $X$ values. This allows the metric to be computed from few samples of image patches, and it also permits histogram estimation with Parzen windows, which can improve the behavior of the cost function. To mitigate

the large spatial intensity inhomogeneity of US images, local CRs are computed from small image patches and are averaged for all the patches $\{\Omega_i\}_{i=1\ldots N_p}$ to form a global cost function as:

$$RaPTOR(X, Y) = \frac{1}{N_p} \sum_{i=1}^{N_p} (1 - \eta(Y|X; \Omega_i)).$$

The nonlinear deformation was modeled with free-form cubic B-splines, and the optimization is achieved through a stochastic gradient descent approach [40] with derivatives of the cost function solved analytically to improve the accuracy and computational speed.

## MRI–US registration

With the optical position tracking system, the US images were acquired in the patient frame of reference, and all the information was stored in the surgical guidance system. The pre-surgical MRI data were rigidly registered to the patient's head using fiducial markers to initialize the MRI–US registration. T2 FLAIR MR images were used for registration since the low-grade gliomas are better visualized. To facilitate registration, the US volumes were first processed with non-local means denoising [41] and then down-sampled to the same resolution as the MRI ($1.0 \times 1.0 \times 1.0\,\text{mm}^3$). Here, we used the US and MRI volumes as the moving and fixed images in our image registration, respectively, and the inverse of the deformation was used to update the pre-surgical data.

## Registration validation

To help quantify brain shift and validate the registration, we identified matching anatomical landmarks between the corresponding MRI and US volumes for each patient. Here, we used the T2 FLAIR MRI to identify the landmarks since it provides better contrast between the tumor and the normal tissue than the T1w MRI. Typical landmarks include the edge of the tumor, grooves of sulci, corners of sulci, and convex points of gyri. There is a limited number of quality and coherent anatomical features that qualify as landmark candidates between MRI and US, and we attempted to identify most of such landmarks. We identified 15 pairs of homologous landmarks for Subjects 1 and 3, and 16 pairs of landmarks for Subjects 2 and 4. These landmarks cover the entire images and are sufficient for validation. To ensure landmark selection quality, two raters performed the task. As Rater 1 defined the reference landmarks in the MRIs, both raters were asked to tag the corresponding landmarks twice in the US volumes. The final landmarks in the US scans are provided as the averaged results of the two trials by both raters. These homologous landmarks were used to compute the mean target registration errors (mTREs) to assess the quality of registration. For $M$ landmark pairs $\{x_i, x_i'\}_{i=1\ldots M}$, the mTRE is computed as

$$mTRE = \frac{1}{M} \sum_{i=1}^{M} ||\mathrm{T}(x_i) - x_i'||,$$

where $T(\cdot)$ represents the spatial transformation and $\|\cdot\|$ computes the Euclidean distance between the two points.

To evaluate the intra- and inter-rater variability, we used the mean Euclidean distance between two sets of corresponding US landmark points for each patient. For intra-rater variability, we calculated the metric between two trials of landmark picking for each rater; for inter-rater variability, the average of two trials for each rater was first obtained and used to compute the metric between two raters.

## Tractography

Each patient's tractography was obtained using MRtrix3 (www.mrtrix.org). First, image denoising [42], field inhomogeneity correction [43], and eddy current correction [44] were performed on the raw diffusion data. The seeding regions of interest (ROIs) for the targeted major white matter fiber bundles near the brain tumors were manually selected based on the color-coded fractional anisotropy (FA) map. Lastly, the tracts were produced with the probabilistic tractography method using the second-order integration over fiber orientation distribution (iFOD2) algorithm [45]. Fiber tracking was stopped when 5,000 tracts reached the selected ROI or when 1000,000 total tracts were generated.

Depending on the tumors' locations, the included tracts were: the cortico-spinal tract (CST), uncinate fasciculus (UNC), inferior fronto-occipital tract (IFO), superior longitudinal fasciculus (SLF), and the tracts passing through the genu of the corpus callosum (CC). Damages to these fiber tracts will affect important brain functions. In addition, we also used the tumor segmentations as ROIs to generate the tracts to observe the infiltration of the cancerous regions, and the connectivity between the tumors and the healthy tissues.

## Surgical data updates due to brain shift

All the surgical data, including T2 FLAIR MRIs, segmented tumors, and the white matter tracts, were nonlinearly warped by deformation fields from MRI–US registration. The results were visualized with the software 3DSlicer [46]. To quantitatively evaluate the changes, we computed the Dice similarity

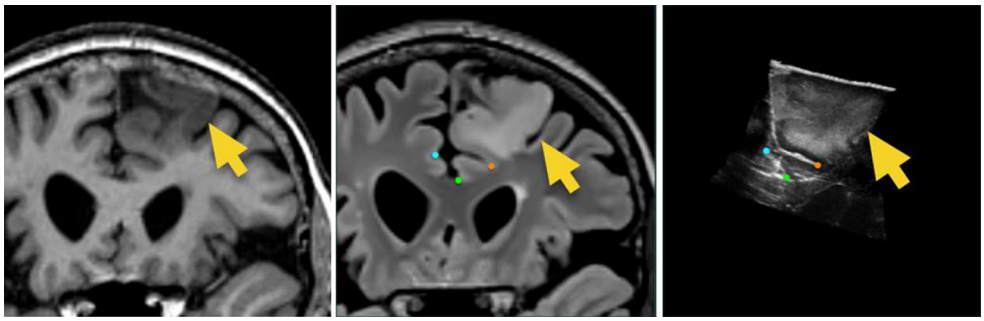

**Fig. 2** Coronal views of T1w MRI (left), T2 FLAIR MRI (middle), and intra-operative ultrasound scan (right). The yellow arrows indicate the tumor, and the corresponding landmarks between T2 FLAIR MRI and ultrasound are shown as colored dots. The ultrasound was aligned to the MRI using landmark-based rigid registration for demonstration purpose

coefficients (DSCs) for the tumor and different fiber bundle volumes between before and after nonlinear deformation. Additionally, for the tumor volumes, we computed the Hausdorff distances between before and after deformation. To offer a better understanding for the impact of brain shift on tractography in terms of displacement, we computed the mean displacement of the fibers in each selected fiber bundle after deformation. To do so, a fiber density map was generated for each fiber bundle in the same resolution of the T2w MRIs and computed deformation fields, and the mean displacement was calculated for all nonzero voxels in the fiber density map.

## Results

### Image characteristics of low-grade gliomas

In T1w MRIs, low-grade gliomas appear dark and calcifications may appear as foci of high T1 signals, while T2 FLAIR images show the contrast between infiltrating tumor (bright signal) margins and normal brain tissues. A comparison of tumor characteristics between MRIs and US for Patient 4 is shown in Fig. 2, along with demonstration of sample landmarks as color-coded dots. Because the contrast between the low-grade gliomas and normal tissues is better in FLAIR images, they are used more actively than T1w MRIs during surgery. In ultrasound, low-grade gliomas are often hyperechoic (brighter than the surrounding white matter).

## MRI–US registration

After registration, the anatomical features between the MRI and US volumes were well aligned. The registration results are shown in Fig. 3, where the T2 FLAIR images are nonlinearly registered to the US volume. The landmark registration errors before and after registration are shown in Table 1. With image registration, the mTRE (mean $\pm$ sd) was reduced from $7.22 \pm 3.35$ to $1.73 \pm 0.62$ mm. Using mTRE as a surrogate for the magnitude of brain shift measurement [47], the severity of the shift (from the least to the most) is ranked as follows: Patient 4, Patient 2, Patient 1, and Patient 3. The evaluation of inter- and intra-rater variability for the quality of landmark selection is listed in Table 2. Although Rater 1 is slightly less consistent in landmark picking, all the measured mean variabilities remain around 0.5 mm, which is half a voxel of the MR image.

**Table 1** Mean target registration errors in mm before and after registration for all patients

| mTRE (mm) | Patient 1 | Patient 2 | Patient 3 | Patient 4 |
|---|---|---|---|---|
| Before | 9.58 | 6.39 | 10.06 | 2.83 |
| After | 1.86 | 1.31 | 2.55 | 1.20 |

## Preoperative tractography

All patients' relevant preoperative white matter fiber bundles along with the segmented tumors are illustrated in Fig. 4. From the results, we observed that some fiber tracts sweep the boundaries of the tumors, while some pass through them, as seen for Patients 2 and 3. For Patient 2, the anterior of the SLF tract originates from the tumor, thus causing the configuration to alter from that seen in healthy subjects. Furthermore, as the tumor interrupts the integrity of the IFO tract, we did not show the particular fiber bundle here. For Patient 3, both the IFO and SLF tracts have some portions within the tumor. As part of the characteristics of low-grade gliomas, the tumor often infiltrates the white matter tracts, instead of complete disruption. Streamlines generated using the tumor segmentations as seeding ROIs before registration are shown in Fig. 5. This approach allows the visualization of directly impacted fibers.

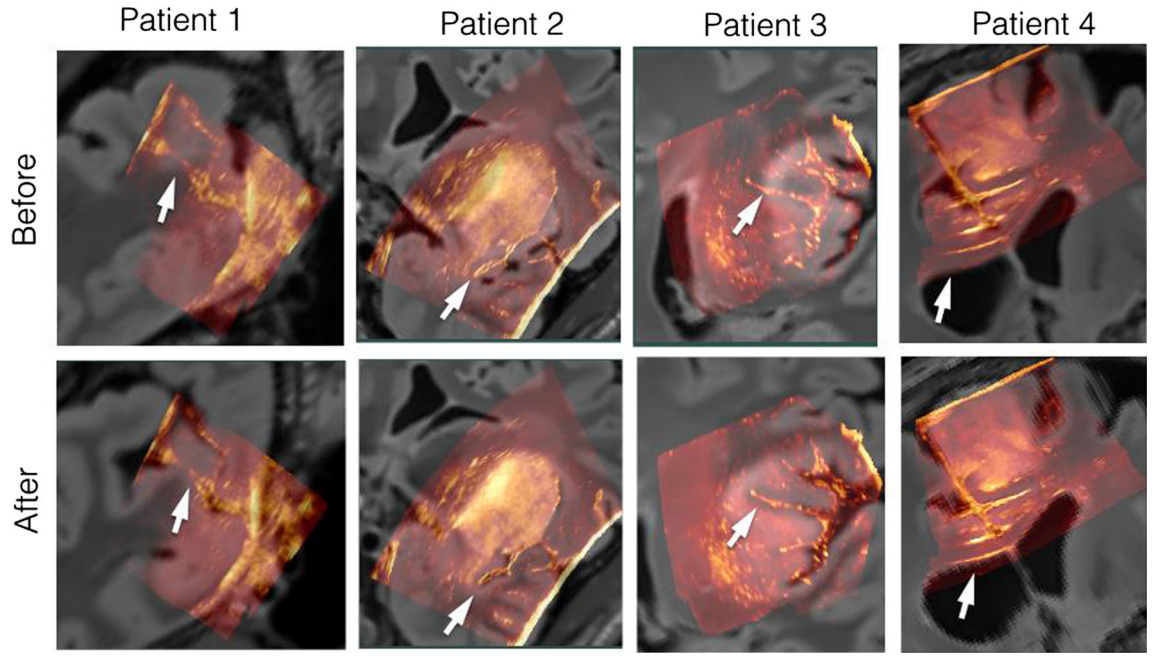


**Fig. 3** Comparison of image alignments before and after nonlinear MRI–US registration for all cases. The first and second row shows ultrasound scans overlaid upon the corresponding MR images before registration and after registration, respectively. After registration, the anatomical features in the US scans (pointed with white arrows) are better aligned with those in the MR images

## Nonlinear deformation of surgical data

To better visualize the impact of the brain shift at surgical sites, in Fig. 6 we rendered the tumor segmentations before and after brain shift as 3D mesh objects in yellow and red, respectively. For Patients 1, 2, and 3, the brain shifts significantly changed the locations of the surgical targets generally toward the direction of gravity. The initial brain shift is relatively small for Patient 4, but misalignment of the tumor before and after tissue shift is still evident. The DSCs for the tumor volumes between before and after deformation are measured at 0.15, 0.70, 0.42, and 0.89 for Patients 1, 2, 3, and 4, respectively. In addition, the Hausdorff distances are measured at 10.68, 8.25, 11.36, and 3.46 mm for Patients 1, 2, 3, and 4, respectively. There is generally less overlap between the tumor volumes in the presence of a more severe brain shift. However, the overlap also depends on the tumor size and position in relation to the tissue deformation.

To show the impact of brain shift on fiber tracts, we color-coded the selected fiber tracts in yellow and blue for before and after deformation, and the results of the previously generated fiber tracts are shown in Figs. 7 and 8. Again, there are visible spatial displacements after brain shift compensation.

For each generated fiber bundle of each patient, we computed the DSC between the regions containing fiber tracts and the mean displacement of fibers before and after accounting for brain shift. The results are listed in Table 3. The metric shows that the position of the fiber bundles can be heavily influenced by brain shift. More particularly, for the UNC tract of Patient 3, there is very little volume overlap (DSC = 0.09) between the pre-surgical plan and after craniotomy, and there is a large mean fiber displacement of 9.93 mm.

**Table 2** Inter- and Intra-rater evaluations with mean Euclidean distances between landmark sets for each patient and mean ± sd values

| | Intra-rater Rater 1 | Intra-rater Rater 2 | Inter-rater R1 versus R2 |
|---|---|---|---|
| Patient 1 | 0.47 mm | 0.24 mm | 0.27 mm |
| Patient 2 | 0.43 mm | 0.40 mm | 0.32 mm |
| Patient 3 | 0.52 mm | 0.31 mm | 0.36 mm |
| Patient 4 | 0.71 mm | 0.26 mm | 0.46 mm |
| Mean ± sd | 0.53 ± 0.12 mm | 0.30 ± 0.07 mm | 0.35 ± 0.08 mm |

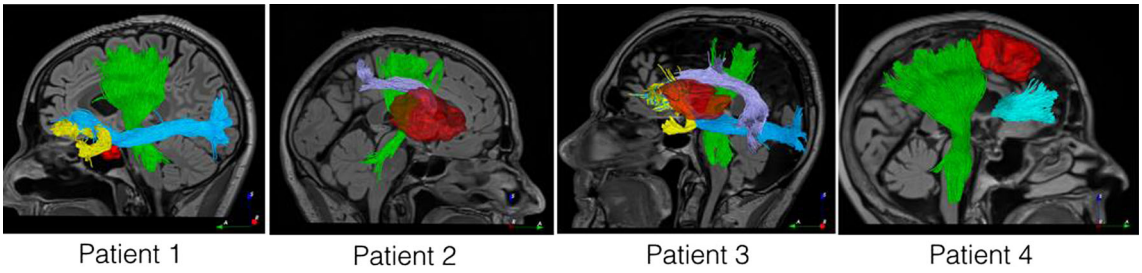


**Fig. 4** Demonstration of preoperative tractography. Tumors are illustrated as red mesh objects. The color coding for different fiber bundles is: green = cortico-spinal tract, yellow = uncinate fasciculus, blue = inferior fronto-occipital tract, purple = superior longitudinal fasciculus, and cyan = tracts passing through the genu of corpus callosum

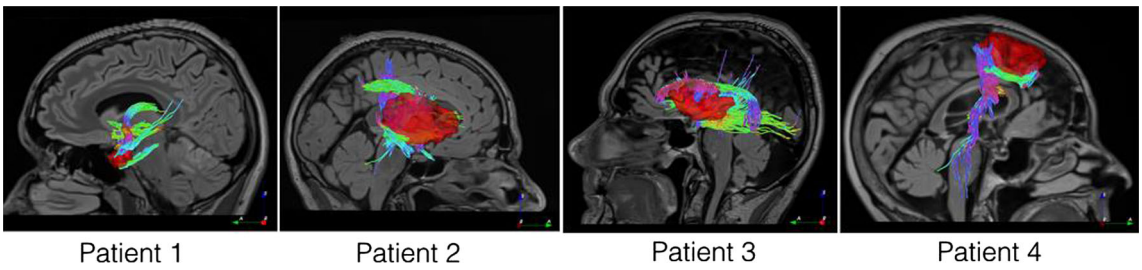


**Fig. 5** Demonstration of fiber tracts obtained using tumor segmentations as regions of interest. The tumors are shown as red mesh objects, and the tracts are color-coded with respect to local fiber segment orientation

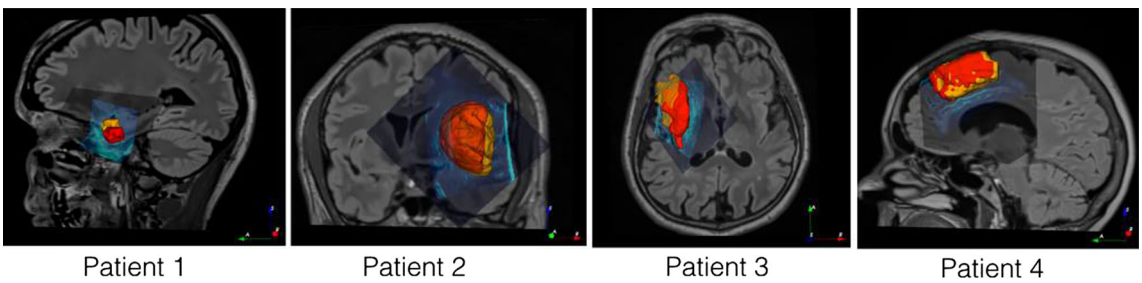


**Fig. 6** Demonstration of tumor deformation after craniotomy. Tumors before and after deformation are shown as semi-transparent yellow and red 3D mesh objects, respectively. The ultrasound scan (in cyan color coding) and deformed MR images are overlaid in the background to help locate the tumors

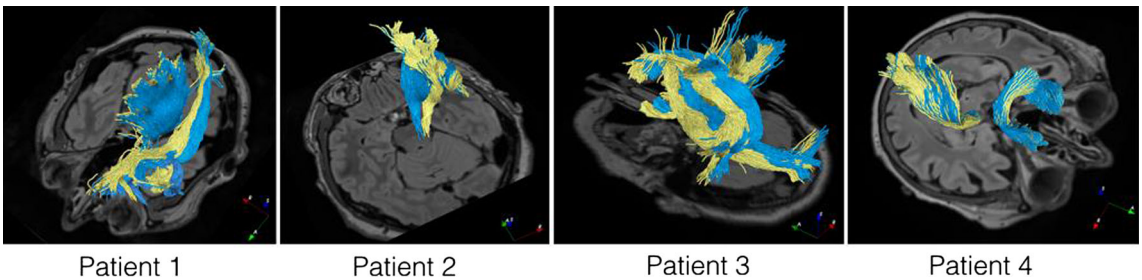


**Fig. 7** Demonstration of tractography deformation for the major white matter fiber bundles. Tracts before and after deformation are shown in yellow and blue colors. Axial T2 FLAIR MRI slices are added to help locate the tracts

## Discussion

Previous studies [48,49] have shown that various types of gliomas interact with the white matter tracts differently. While high-grade gliomas primarily disrupt the tracts, low-grade gliomas infiltrate tracts along myelinated fibers. These changes cause the tractography and the DTI-related measurements (e.g., fractional anisotropy) to alter from the healthy

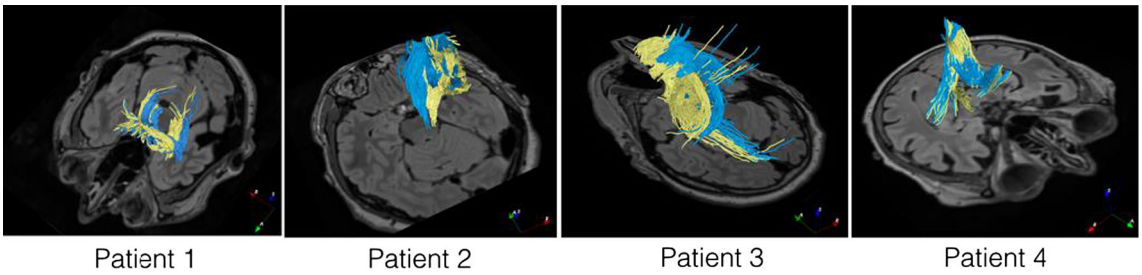


**Fig. 8** Demonstration of tractography deformation using tracts generated with tumor volumes as ROIs. Tracts before and after deformation are shown in yellow and blue colors. Axial T2 FLAIR MRI slices are added to help locate the tracts

**Table 3** Dice similarity coefficients (DSCs) and mean fiber displacements (shown in square brackets) between fiber bundles before and after nonlinear deformation

| | Patient 1 | Patient 2 | Patient 3 | Patient 4 |
|---|---|---|---|---|
| CST | 0.45 [4.58 mm] | 0.53 [6.72 mm] | 0.10 [10.70 mm] | 0.87 [1.19 mm] |
| UNC | 0.21 [8.06 mm] | | 0.09 [9.93 mm] | |
| IFO | 0.44 [5.30 mm] | | 0.21 [9.45 mm] | |
| SLF | | 0.57 [5.03 mm] | 0.21 [10.05 mm] | |
| CC-genu | | | | 0.93 [1.96 mm] |
| Tumor-ROI | 0.31 [6.71 mm] | 0.36 [7.49 mm] | 0.13 [10.34 mm] | 0.82 [2.27 mm] |

*CST* cortico-spinal tract, *UNC* uncinate fasciculus, *IFO* inferior fronto-occipital tract, *SLF* superior longitudinal fasciculus, *CC-genu* tracts passing through the genu of corpus callosum, *Tumor-ROI* fiber tracking using tumor segmentation as ROI

brains in the involved regions. Although diffusion imaging can help characterize the tumorous tissues, we only focused on the registration of tractography in this article. By qualitatively visualizing the tractography and quantitatively measuring the volume overlap (i.e., DSC) and fiber displacements before and after brain shift compensation, we have observed large discrepancies between them. This confirms the need to provide updated tracts as the surgery progresses, offering the surgeon sufficient information during resection. This is especially true for low-grade gliomas, which still contain certain intact white matter tracts. Overall, the deformation appears more profound around the tumors and is generally toward the gravity. However, the movement can be complex due to many factors, including the pressure from the transducer (the probe pressure is very small), size of the craniotomy, tumor texture and locations. In this work, we demonstrated our technique to track tractography deformation for the initial tissue shift before opening the dura because the initial tissue shift often sets the tone for the rest of the surgery. In our future studies, we will explore brain shift correction to monitor tractography deformation during the rest of the surgery stages.

With RaPTOR [38], we are able to effectively reduce the mean landmark registration errors between the preoperative MRI and intra-operative US. Currently, RaPTOR is implemented as a MATLAB (MathWorks, Inc., Natick, USA) software package, and the MRI–US registration is performed using a MacBook Pro with a 3.1 GHz Intel Core i7 and 16 GM RAM. As the acquired US volumes have a relatively small coverage, the registration was conducted primarily at $1 \times 1 \times 1\,\text{mm}^3$ resolution with the whole brain volume to cover all the potential white matter tracts. Registration was completed in about 20 min. Brain tumor resection typically takes a few hours, so this running time should be reduced by approximately a factor of two to be clinically relevant. This speed up is easily achievable by parallel implementation of RaPTOR or implementation in C++. In this study, we used 3D US volumes for MRI–US registration. The volumes were reconstructed from spatially tracked 2D US scans, instead of directly from a 3D US transducer. Alternatively, direct multislice-to-volume registration strategies [50] may also be employed to improve the computational efficiency.

In this paper, we employed an established clinical DWI protocol to produce the white matter tracts, which has been integrated in planning brain tumor resection at the St. Olavs University Hospital. Although it is true that more advanced imaging techniques, such as high angular resolution diffusion-weighted imaging (HARDI) [51] and its variants, can further improve the accuracy of fiber tracking, they are still rarely seen in the clinic, primarily due to time and hardware constraints. This work showed that clinical DWI, which is more widely available than research-grade DWI, can be used in conjunction with intra-operative ultrasound, and with future improvements on DWI protocols, the proposed technique can potentially provide more accurate information during resection. Considering the scarcity of functional data in conjunction with intra-operative images in

brain tumor resection, to the best of our knowledge, this work is the first to explicitly demonstrate the technique to track nonlinear deformation of white matter tracts in ultrasound-guided tumor resection with real clinical cases. Here, we used four clinical cases for our experiments. Among them, there are sufficient variabilities in the severity of brain shift, tumor locations, and sizes so that the preliminary results will lead to a better demonstration of the workflow, which we will evaluate with more clinical cases in the future. We used DSC and mean fiber displacements to quantify the potential impact of brain shift on white matter tracts during surgery and showed the need to update the tracts information along with the tumor volume. While the landmark-based registration errors can on some level reflect the accuracy of tracking tractography deformation, it is still challenging to validate tractography deformation as additional ground truth data are hard to acquire. One way to cross-validate the quality of tractography deformation estimation with the help of MRI–US registration is by obtaining DWI data throughout the surgery in conjunction with intra-operative MRI. However, this technology is still rare in the clinic, and intra-operative MRI is often of lower image quality, which may adversely affect the quality of the comparison. In addition, electrophysiological data [52] during resection can help further confirm the technique introduced in this work. We will conduct more thorough validation with these techniques in the future.

## Conclusions

As a relatively new imaging modality for surgical planning, diffusion imaging offers functional information that is important to guide the resection of brain tumors. Thanks to intra-operative ultrasound and robust image registration techniques, we can track and correct the brain shift during resection and thus update the surgical plan. We have retrospectively demonstrated the technique to track nonlinear deformation of pre-surgical tractography for four low-grade glioma patients who underwent tumor surgeries, and the results revealed the need for updating the white matter tracts during surgery. This is the first step toward incorporating functional data in intra-operative monitoring to help potentially improve the quality and outcomes of tumor resection.

**Acknowledgements** This project was partly funded by NSERC Discovery Grant and the Norwegian National Advisory Unit for Ultrasound and Image-Guided Therapy. The authors thank Dr. Maryse Fortin for her generous help in identifying the anatomical landmarks.

### Compliance with ethical standards

**Conflict of interest** Yiming Xiao, Live Eikenes, Ingerid Reinertsen, and Hassan Rivaz declare that they have no conflict of interest.

**Ethical standard** All procedures performed in studies involving human participants were in accordance with the ethical standards of the institutional and/or national research committee and with the 1964 Declaration of Helsinki and its later amendments or comparable ethical standards.

**Informed consent** Informed consent was obtained from all participants included in the study.

## References

1. Holland EC (2001) Progenitor cells and glioma formation. Curr Opin Neurol 14:683–688
2. Schwartzbaum JA, Fisher JL, Aldape KD, Wrensch M (2006) Epidemiology and molecular pathology of glioma. Nat Clin Pract Neurol 2:494–503 quiz 491 p following 516
3. Louis DN, Ohgaki H, Wiestler OD, Cavenee WK, Burger PC, Jouvet A, Scheithauer BW, Kleihues P (2007) The 2007 WHO classification of tumours of the central nervous system. Acta Neuropathol 114:97–109
4. Dolecek TA, Propp JM, Stroup NE, Kruchko C (2012) CBTRUS statistical report: primary brain and central nervous system tumors diagnosed in the United States in 2005–2009. Neuro Oncol 14(Suppl 5):v1–49
5. Jakola AS, Myrmel KS, Kloster R, Torp SH, Lindal S, Unsgard G, Solheim O (2012) Comparison of a strategy favoring early surgical resection vs a strategy favoring watchful waiting in low-grade gliomas. J Am Med Assoc 308:1881–1888
6. Schomas DA, Laack NNI, Rao RD, Meyer FB, Shaw EG, O'Neill BP, Giannini C, Brown PD (2009) Intracranial low-grade gliomas in adults: 30-year experience with long-term follow-up at Mayo Clinic. Neuro-Oncology 11:437–445
7. Nimsky C, Ganslandt O, Merhof D, Sorensen AG, Fahlbusch R (2006) Intraoperative visualization of the pyramidal tract by diffusion-tensor-imaging-based fiber tracking. Neuroimage 30:1219–1229
8. Stadlbauer A, Ganslandt O, Buslei R, Hammen T, Gruber S, Moser E, Buchfelder M, Salomonowitz E, Nimsky C (2006) Gliomas: histopathologic evaluation of changes in directionality and magnitude of water diffusion at diffusion-tensor MR imaging. Radiology 240:803–810
9. Maurer CR, Hill DLG, Martin AJ, Liu HY, McCue M, Rueckert D, Lloret D, Hall WA, Maxwell RE, Hawkes DJ, Truwit CL (1998) Investigation of intraoperative brain deformation using a 1.5-t interventional MR system: preliminary results. IEEE Trans Med Imaging 17:817–825
10. Bucholz RD, Yeh DD, Trobaugh J, McDurmont LL, Sturm CD, Baumann C, Henderson JM, Levy A, Kessman P (1997) The correction of stereotactic inaccuracy caused by brain shift using an intraoperative ultrasound device. Lect Notes Comput Sci 1205:459–466
11. Nimsky C, Ganslandt O, Cerny S, Hastreiter P, Greiner G, Fahlbusch R (2000) Quantification of, visualization of, and compensation for brain shift using intraoperative magnetic resonance imaging. Neurosurgery 47:1070–1079
12. Haberg A, Kvistad KA, Unsgard G, Haraldseth O (2004) Preoperative blood oxygen level-dependent functional magnetic resonance imaging in patients with primary brain tumors: clinical application and outcome. Neurosurgery 54:902–914 **(discussion 914-905)**
13. Rasmussen IA Jr, Lindseth F, Rygh OM, Berntsen EM, Selbekk T, Xu J, Nagelhus Hernes TA, Harg E, Haberg A, Unsgaard G (2007) Functional neuronavigation combined with intra-operative 3D ultrasound: initial experiences during surgical resections close to eloquent brain areas and future directions in automatic brain shift compensation of preoperative data. Acta Neurochir 149:365–378

14. Stapleton SR, Kiriakopoulos E, Mikulis D, Drake JM, Hoffman HJ, Humphreys R, Hwang P, Otsubo H, Holowka S, Logan W, Rutka JT (1997) Combined utility of functional MRI, cortical mapping, and frameless stereotaxy in the resection of lesions in eloquent areas of brain in children. Pediatr Neurosurg 26:68–82
15. Al-Okaili RN, Krejza J, Woo JH, Wolf RL, O'Rourke DM, Judy KD, Poptani H, Melhem ER (2007) Intraaxial brain masses: MR imaging-based diagnostic strategy—initial experience. Radiology 243:539–550
16. Lu S, Ahn D, Johnson G, Law M, Zagzag D, Grossman RI (2004) Diffusion-tensor MR imaging of intracranial neoplasia and associated peritumoral edema: introduction of the tumor infiltration index. Radiology 232:221–228
17. Roldan-Valadez E, Rios C, Cortez-Conradis D, Favila R, Moreno-Jimenez S (2014) Global diffusion tensor imaging derived metrics differentiate glioblastoma multiforme vs. normal brains by using discriminant analysis: introduction of a novel whole-brain approach. Radiol Oncol 48:127–136
18. Nimsky C, Ganslandt O, Fahlbusch R (2007) Implementation of fiber tract navigation. Neurosurgery 61:306–317 **(discussion 317-308)**
19. Romano A, D'Andrea G, Minniti G, Mastronardi L, Ferrante L, Fantozzi LM, Bozzao A (2009) Pre-surgical planning and MR-tractography utility in brain tumour resection. Eur Radiol 19:2798–2808
20. Lu JF, Zhang H, Wu JS, Yao CJ, Zhuang DX, Qiu TM, Jia WB, Mao Y, Zhou LF (2013) "Awake" intraoperative functional MRI (ai-fMRI) for mapping the eloquent cortex: Is it possible in awake craniotomy? Neuroimage Clin 2:132–142
21. Nimsky C, Ganslandt O, Hastreiter P, Wang R, Benner T, Sorensen AG, Fahlbusch R (2005) Intraoperative diffusion-tensor MR imaging: shifting of white matter tracts during neurosurgical procedures-initial experience. Radiology 234:218–225
22. Steno A, Karlik M, Mendel P, Cik M, Steno J (2012) Navigated three-dimensional intraoperative ultrasound-guided awake resection of low-grade glioma partially infiltrating optic radiation. Acta Neurochir 154:1255–1262
23. Intraoperative ultrasound (ious) in neurosurgery: from standard b-mode to elastosonography. Springer, Berlin (2016)
24. Roche A, Pennec X, Malandain G, Ayache N (2001) Rigid registration of 3-D ultrasound with MR images: a new approach combining intensity and gradient information. IEEE Trans Med Imaging 20:1038–1049
25. Mercier L, Fonov V, Haegelen C, Del Maestro RF, Petrecca K, Collins DL (2012) Comparing two approaches to rigid registration of three-dimensional ultrasound and magnetic resonance images for neurosurgery. Int J Comput Assist Radiol Surg 7:125–136
26. Arbel T, Morandi X, Comeau RM, Collins DL (2004) Automatic non-linear MRI-ultrasound registration for the correction of intra-operative brain deformations. Comput Aided Surg 9:123–136
27. Collins DL, Neelin P, Peters TM, Evans AC (1994) Automatic 3D intersubject registration of MR volumetric data in standardized Talairach space. J Comput Assist Tomogr 18:192–205
28. Kuklisova-Murgasova M, Cifor A, Napolitano R, Papageorghiou A, Quaghebeur G, Rutherford MA, Hajnal JV, Noble JA, Schnabel JA (2013) Registration of 3D fetal neurosonography and MRI. Med Image Anal 17:1137–1150
29. Mellor M, Brady M (2005) Phase mutual information as a similarity measure for registration. Med Image Anal 9:330–343
30. De Nigris D, Collins DL, Arbel T (2012) Multi-modal image registration based on gradient orientations of minimal uncertainty. IEEE Trans Med Imaging 31:2343–2354
31. Reinertsen I, Lindseth F, Unsgaard G, Collins DL (2007) Clinical validation of vessel-based registration for correction of brain-shift. Med Image Anal 11:673–684
32. Reinertsen I, Descoteaux M, Siddiqi K, Collins DL (2007) Validation of vessel-based registration for correction of brain shift. Med Image Anal 11:374–388
33. Coupe P, Hellier P, Morandi X, Barillot C (2012) 3D rigid registration of intraoperative ultrasound and preoperative MR brain images based on hyperechogenic structures. Int J Biomed Imaging 2012:531319
34. Ji SB, Wu ZJ, Hartov A, Roberts DW, Paulsen KD (2008) Mutual-information-based image to patient re-registration using intraoperative ultrasound in image-guided neurosurgery. Med Phys 35:4612–4624
35. Wein W, Ladikos A, Fuerst B, Shah A, Sharma K, Navab N (2013) Global registration of ultrasound to MRI using the LC2 metric for enabling neurosurgical guidance. In: Medical image computing and computer-assisted intervention (Miccai 2013), Pt I 8149, pp 34–41
36. Fuerst B, Wein W, Muller M, Navab N (2014) Automatic ultrasound-MRI registration for neurosurgery using the 2D and 3D LC2 Metric. Med Image Anal 18:1312–1319
37. Ferrante E, Paragios N (2013) Non-rigid 2D–3D medical image registration using Markov random fields. In: Medical image computing and computer-assisted intervention (Miccai 2013), Pt Iii 8151, pp 163–170
38. Rivaz H, Chen SJS, Collins DL (2015) Automatic deformable MR-ultrasound registration for image-guided neurosurgery. IEEE T Med Imaging 34:366–380
39. Roche A, Malandain G, Pennec X, Ayache N (1998) The correlation ratio as a new similarity measure for multimodal image registration. In: Medical image computing and computer-assisted intervention—Miccai'98 1496, pp 1115–1124
40. Klein S, Pluim JPW, Staring M, Viergever M (2009) Adaptive stochastic gradient descent optimisation for image registration. Int J Comput Vision 81:227–239
41. Coupe P, Yger P, Prima S, Hellier P, Kervrann C, Barillot C (2008) An optimized blockwise nonlocal means denoising filter for 3-D magnetic resonance images. IEEE Trans Med Imaging 27:425–441
42. Veraart J, Novikov DS, Christiaens D, Ades-Aron B, Sijbers J, Fieremans E (2016) Denoising of diffusion MRI using random matrix theory. Neuroimage 142:384–396
43. Smith SM, Jenkinson M, Woolrich MW, Beckmann CF, Behrens TEJ, Johansen-Berg H, Bannister PR, De Luca M, Drobnjak I, Flitney DE, Niazy RK, Saunders J, Vickers J, Zhang YY, De Stefano N, Brady JM, Matthews PM (2004) Advances in functional and structural MR image analysis and implementation as FSL. Neuroimage 23:S208–S219
44. Andersson JL, Sotiropoulos SN (2016) An integrated approach to correction for off-resonance effects and subject movement in diffusion MR imaging. Neuroimage 125:1063–1078
45. Tournier J-D, Calamante F, Connelly A (2010) Improved probabilistic streamlines tractography by 2nd order integration over fibre orientation distributions. In: Proceedings of the international society for magnetic resonance in medicine 1670
46. Fedorov A, Beichel R, Kalpathy-Cramer J, Finet J, Fillion-Robin JC, Pujol S, Bauer C, Jennings D, Fennessy F, Sonka M, Buatti J, Aylward S, Miller JV, Pieper S, Kikinis R (2012) 3D Slicer as an image computing platform for the Quantitative Imaging Network. Magn Reson Imaging 30:1323–1341
47. Gerard IJ, Kersten-Oertel M, Petrecca K, Sirhan D, Hall JA, Collins DL (2017) Brain shift in neuronavigation of brain tumors: a review. Med Image Anal 35:403–420
48. Campanella M, Ius T, Skrap M, Fadiga L (2014) Alterations in fiber pathways reveal brain tumor typology: a diffusion tractography study. PeerJ 2:e497
49. Papageorgiou TS, Chourmouzi D, Drevelengas A, Kouskouras K, Siountas A (2015) Diffusion tensor imaging in brain tumors: a study on gliomas and metastases. Phys Med 31:767–773

50. Ferrante E, Paragios N (2017) Slice-to-volume medical image registration: a survey. Med Image Anal 39:101–123
51. Tuch DS, Reese TG, Wiegell MR, Makris N, Belliveau JW, Wedeen VJ (2002) High angular resolution diffusion imaging reveals intravoxel white matter fiber heterogeneity. Magn Reson Med 48:577–582
52. Duffau H (2017) Mapping the connectome in awake surgery for gliomas: an update. J Neurosurg Sci 61:612–630